

RESOLVING THE INTERNAL STRUCTURE OF CIRCUM-GALACTIC MEDIUM USING GRAVITATIONALLY LENSED QUASARS¹

SUZUKA KOYAMADA², TORU MISAWA³, NAOHISA INADA⁴, MASAMUNE OGURI^{5,6,7}, NOBUNARI KASHIKAWA^{8,9}, KATSUYA OKOSHI¹⁰

¹Based on data collected at Subaru Telescope, which is operated by the National Astronomical Observatory of Japan.

²Department of Physics, Faculty of Science, Shinshu University, 3-1-1 Asahi, Matsumoto, Nagano 390-8621 Japan, e-mail: szk.koyamada@gmail.com

³School of General Education, Shinshu University, 3-1-1 Asahi, Matsumoto, Nagano 390-8621, Japan

⁴Department of Physics, Nara National College of Technology, Yamatokohriyama, Nara 639-1080, Japan

⁵Research Center for the Early Universe, University of Tokyo, 7-3-1 Hongo, Bunkyo-ku, Tokyo 113-0033, Japan

⁶Department of Physics, University of Tokyo, 7-3-1 Hongo, Bunkyo-ku, Tokyo 113-0033, Japan

⁷Kavli Institute for the Physics and Mathematics of the Universe (Kavli IPMU, WPI), University of Tokyo, Chiba 277-8583, Japan

⁸Department of Astronomy, School of Science, SOKENDAI (The Graduate University for Advanced Studies), Mitaka, Tokyo 181-8588, Japan

⁹Optical and Infrared Astronomy Division, National Astronomical Observatory of Japan, Mitaka, Tokyo 181-8588, Japan and

¹⁰Tokyo University of Science, 102-1 Tomino, Oshamambe, Hokkaido, 049-3514, Japan

Draft version November 23, 2017

ABSTRACT

We study the internal structure of the Circum-Galactic Medium (CGM), using 29 spectra of 13 gravitationally lensed quasars with image separation angles of a few arcseconds, which correspond to 100 pc to 10 kpc in physical distances. After separating metal absorption lines detected in the spectra into high-ions with ionization parameter (IP) > 40 eV and low-ions with IP < 20 eV, we find that i) the fraction of absorption lines that are detected in only one of the lensed images is larger for low-ions (~16%) than high-ions (~2%), ii) the fractional difference of equivalent widths (*EW*s) between the lensed images is almost same (*dEW* ~ 0.2) for both groups although the low-ions have a slightly larger variation, and iii) weak low-ion absorbers tend to have larger *dEW* compared to weak high-ion absorbers. We construct simple models to reproduce these observed properties and investigate the distribution of physical quantities such as size and location of absorbers, using some free parameters. Our best models for absorbers with high-ions and low-ions suggest that i) an overall size of the CGM is at least ~ 500 kpc, ii) a size of spherical clumpy cloud is ~ 1 kpc or smaller, and iii) only high-ion absorbers can have diffusely distributed homogeneous component throughout the CGM. We infer that a high ionization absorber distributes almost homogeneously with a small-scale internal fluctuation, while a low ionization absorber consists of a large number of small-scale clouds in the diffusely distributed higher ionized region. This is the first result to investigate the internal small-scale structure of the CGM, based on the large number of gravitationally lensed quasar spectra.

Subject headings: galaxies:formation – intergalactic medium

1. INTRODUCTION

Cosmologically intervening metal absorbers detected in spectra of background quasars (e.g., Lanzetta & Bowen 1990; Bergeron & Boissé 1991) and galaxies (e.g., Adelberger et al. 2005; Steidel et al. 2010) are good probes of the Circum-Galactic Medium (CGM) of foreground galaxies. The CGM, which is fuel for star formation in the galaxy and/or ejected matter blown out by galactic winds, recently attracts a lot of attention as it is a key ingredient to understand galaxy formation and evolution. Based on multiple galaxy-CGM spectroscopy, the radial gradient of equivalent width (*EW*) and column density ($\log N$) of both hydrogen and metal absorbers in the CGM as a function of transverse and line-of-sight directions were built up to several proper Mpc (pMpc, hereafter) from galaxies at $z_{\text{abs}} < 0.5$ (e.g., Chen et al. 2010a,b; Tumlinson et al. 2011; Prochaska et al. 2011; Werk et al. 2016) and at $z_{\text{abs}} \sim 2 - 3$ (e.g., Rakic et al. 2012, 2013; Turner et al. 2014, 2015; Rubin et al. 2015). Several studies have revealed the radial gradient of physical conditions in the CGM such as covering factor (C_f), ionization parameter ($\log U$), gas

temperature (T_{gas}), and turbulence velocity (v_{turb}) (e.g., Rudie et al. 2012; Rakic et al. 2012; Prochaska et al. 2013; Turner et al. 2014; Lau et al. 2015). Recently, projected 2D maps along our sightline have also been built through multi-sightline spectroscopy (Prochaska et al. 2014; Stern et al. 2016), deep narrow-band imaging (Cantalupo et al. 2014; Hennawi et al. 2015) and integral field spectroscopy (e.g., Borisova et al. 2016). Arrigoni Battaia et al. (2016) suggested that diffuse Ly α emission from the CGM could distribute up to ~ 500 proper kpc (pkpc, hereafter) from quasar host galaxies with a detection limit of $\text{SB}_{\text{Ly}\alpha} = 5.5 \times 10^{-20} \text{ erg s}^{-1} \text{ cm}^{-2} \text{ arcsec}^{-2}$. Thus, a *global* picture of the CGM is being formed progressively. On the other hand, very little has been known about an *internal* small scale structure of the CGM, such as i) their homogeneity or clumpiness, and ii) a typical scale of each clumpy cloud (or density fluctuation) if the latter is the case. One of the difficulty to probe the CGM internal structure is that only one-dimensional distribution can basically be drawn using a background spectrum.

Gravitationally lensed quasars are powerful tools for

TABLE 1
SAMPLE QUASARS

Lensed QSO	z_{em}^a	z_l^b	θ^c (arcsec)	Instrument	λ -coverage (Å)	$\lambda/\Delta\lambda^d$	T_{exp} (sec)	Reference ^e
(1)	(2)	(3)	(4)	(5)	(6)	(7)	(8)	(9)
SDSS J024634.11−082536.2	1.686	0.724	1.04	Keck/ESI	3900 − 11000	~ 27000	900	1
SDSS J074653.03+440351.3	1.998	0.513	1.08	Keck/ESI	3900 − 11000	~ 27000	1200	2
SDSS J080623.70+200631.9	1.538	0.573	1.49	Keck/ESI	3900 − 11000	~ 27000	900	3
SDSS J090404.15+151254.5	1.826	~ 0.30	1.13	Gemini/GMOS	3700 − 9800	~ 1000	4200	4
SDSS J092455.87+021924.9	1.523	0.394	1.81	Keck/ESI	3900 − 11000	~ 27000	1200	5
SDSS J100128.61+502756.8	1.841	0.415	2.86	Gemini/GMOS	3700 − 9800	~ 1000	4800	6
SDSS J113157.72+191527.7	2.915	~ 0.30	1.46	Gemini/GMOS	3700 − 9800	~ 1000	4800	4
SDSS J125819.24+165717.6	2.702	0.505	1.28	Gemini/GMOS	3700 − 9800	~ 1000	4800	7
SDSS J134929.84+122706.8	1.722	~ 0.65	3.00	Gemini/GMOS	3700 − 9800	~ 1000	3600	4
SDSS J135306.35+113804.7	1.624	~ 0.25	1.41	Keck/ESI	3900 − 11000	~ 27000	600	3
HE1104−1805	2.319	0.73	3.19	3.9m-AAT/RGO	3170 − 7570	~ 12000	~ 5200	8
H1413+1143	2.551	~ 1.88	0.76, 0.86, 1.10	HST/FOS	3250 − 6500	~ 1300	~ 4600	9
APM08279+5255	3.911	1.06	0.15, 0.38	HST/STIS	5970 − 8600	~ 5000	~ 14900	10

^a Quasar emission redshift.

^b Redshift of a foreground lensing galaxy. Approximate values are photometric redshifts rather than spectroscopic redshifts.

^c Separation angle between lensed images seen from us in arcsec.

^d Spectral resolution

^e References — 1: Inada et al. 2005, 2: Inada et al. 2007, 3: Inada et al. 2006, 4: Kayo et al. 2010, 5: Inada et al. 2003, 6: Oguri et al. 2005, 7: Inada et al. 2009, 8: Smette et al. 1995, 9: Monier et al. 1998, and 10: Ellison et al. 2004.

investigating an internal structure of the CGM. A typical separation angle of lensed images is a few to tens of arcseconds, corresponding to 100 pc to 100 kpc¹ between two paths at $z \sim 1.0 - 4.0$ based on a standard cosmological model. This kind of observations have already been partially performed for investigating cosmologically intervening absorbers (e.g., Smette et al. 1995; Monier et al. 1998). For example, based on spectra of the triply imaged quasar APM08279 + 5255, Ellison et al. (2004) suggested an important trend that : H I absorbers and high ionization systems like C IV absorbers show coherence (i.e. coincidence) on the multiple sightlines over distances of $\sim 100 - 300$ kpc, while low ionization systems like Mg II exhibit significant sightline-variation on scales greater than a few hundred parsec. This is qualitatively consistent with a simple picture of clumpy, low ionization gas, embedded in homogeneous, highly ionized outer halos. These trends are also reminiscent of the hierarchical structure formation (e.g., Stern et al. 2016). However, sample sizes of the past studies (i.e., only a few lensed-quasars) are not large enough for statistical analysis.

In this paper, we collected a (large) sample of spectra of gravitationally lensed quasars to statistically study an internal structure of the CGM through comparisons of parameters, including absorption detection rate and rest-frame equivalent widths (REW) as a function of ionization condition and physical separation between lensed images. Because our goal is to resolve the internal small-scale structure of the CGM, we do not necessarily need to know the positions of the galaxies hosting the CGM giving rise to the absorption lines with respect to the background gravitationally lensed quasars. In §2, we describe the data sample and the methods used for detecting absorption lines and measuring their parameters. The results and discussion are presented in §3 and §4, respectively. We summarize our results in §5. We use a cosmology with $H_0 = 70 \text{ km s}^{-1} \text{ Mpc}^{-1}$, $\Omega_m = 0.3$, and

¹ The largest separation distance corresponds to large-separation lensed quasars by a cluster of galaxies with a separation angle of $\theta > 10$ arcsec.

$\Omega_\Lambda = 0.7$ throughout the paper.

2. DATA AND ANALYSIS

We select our sample quasars from the Sloan Digital Sky Survey Quasar Lens Search (SQLS; Inada et al. 2012; Oguri et al. 2012 and reference therein). The SQLS repeatedly performed spectroscopic observations for gravitationally lensed quasar candidates with various telescopes and instruments, and discovered 62 lensed quasars. Because the quality of observed spectra (e.g., wavelength coverage, resolution, and signal-to-noise (S/N)-ratio) is heterogeneous, we select lensed quasars whose spectra satisfy all the following criteria: a) C IV and Mg II absorption lines are covered by optical spectra (i.e., quasar emission redshift is larger than 1.5), b) spectral resolution is greater than 1000, c) wavelength coverage is wide enough to cover from $\sim 4,000 \text{ Å}$ to $\sim 1 \mu\text{m}$, d) data quality is high enough (i.e., an S/N-ratio is greater than $\sim 20 \text{ pixel}^{-1}$ on average after sampling in a spectrum). We use 20 spectra of 10 lensed quasars taken with Keck/ESI (wavelength resolution is $\lambda/\Delta\lambda \sim 27000$) or Gemini/GMOS ($\lambda/\Delta\lambda \sim 1000$) from SQLS that satisfy the criteria described above (see Table 1). Although the spectral resolution is very different between those taken with Keck/ESI and Gemini/GMOS, their pixel scale after sampling is almost same, $\sim 1.8 \text{ Å pix}^{-1}$. We also confirmed the effect of self-blending (i.e., blue and red members of doublet are blended each other because of low spectral resolution) is not important when we measure equivalent width later.² We define the brighter quasar image as image 1, the fainter as image 2 in optical bands. Parameters of absorption lines detected in each lensed image are shown with subscript 1 or 2, hereafter.

² We synthesized spectra of C IV doublet using typical line parameters of $z_{\text{abs}} = 2.0$, column density $\log N = 14.0 \text{ cm}^{-2}$, and Doppler parameter $b = 50 \text{ km s}^{-1}$ with pixel scale of 1.8 Å pix^{-1} , S/N ratio of 20 pix^{-1} , and two spectral resolutions of $\lambda/\Delta\lambda = 1000$ and 27000 . Although the doublet is self-blended only in the $\lambda/\Delta\lambda = 1000$ spectrum, we confirmed their total equivalent widths are almost same.

In our spectra, we detect all absorption features (except for heavily blended ones) whose absorption depths at the center are greater than 5 times of noise level using the code SEARCH (Churchill 1997; Churchill et al. 2003). Then, we identify doublet lines such as C iv, Si iv, and Mg ii in the spectral region between Ly α and the corresponding emission lines. We also search for other single metal lines at the same redshift as the doublet lines above.

For all detected doublets, we measure absorption redshifts (z_1, z_2) and rest-frame equivalent widths (REW_1, REW_2) with their 1σ uncertainties ($\sigma(REW_1), \sigma(REW_2)$)³, in the spectra of both lensed images. Because blue and red members of doublet are sometimes blended each other especially for the low resolution spectra taken with Gemini/GMOS ($\lambda/\Delta\lambda \sim 1000$), we calculate *total REWs* of two transitions, C iv $\lambda\lambda$ 1548, 1551 (C iv 1550, hereafter) and Mg ii $\lambda\lambda$ 2796, 2803 (Mg ii 2800, hereafter) including both doublet members. We chose C iv and Mg ii doublets as representative transitions for high and low-ionization transitions because these doublets are most frequently detected among each category. We also measure above parameters for the other metal lines.

We also calculate the physical separation in the transverse direction (D_{tra})⁴ and the fractional equivalent width difference (Ellison et al. 2004) defined by

$$dEW = \frac{|REW_1 - REW_2|}{\max(REW_1, REW_2)}. \quad (1)$$

Because absorption strength is enhanced (compared to the intergalactic medium) around galaxies up to $\Delta v \sim 240 \text{ km s}^{-1}$ along the line-of-sight for H i and metal absorption lines including C iv (Turner et al. 2014), we assume absorption lines within 400 km s^{-1} (i.e., $\leq 240 \times 2 \text{ km s}^{-1}$) each other into a single absorption “system”. As a result, we detected 30 C iv, 8 Si iv, 39 Mg ii doublets as well as 46 single metal lines in 36 absorption systems in total (see Table 2).

In addition to our data, we also include similar measurements from the literature for our statistical analysis: double images of HE1104–1805 (a quasar emission redshift is $z_{\text{em}} = 2.319$, a redshift of lensing galaxy is $z_1 = 0.73$, and a separation angle is $\theta = 3''.19$) taken with 3.9m-AAT/RGO ($\lambda/\Delta\lambda \sim 12000$, $\lambda = 3200 - 7500 \text{ \AA}$; Smette et al. 1995), quartet images of H1413+1143 ($z_{\text{em}} = 2.551$, $z_1 = 1.88$, $\theta = 1''.10$) taken with HST/FOS ($\lambda/\Delta\lambda \sim 1300$, $\lambda = 3200 - 6500 \text{ \AA}$; Monier et al. 1998), and triple images of APM08279+5255 ($z_{\text{em}} = 3.911$, $z_1 = 1.062$, $\theta = 0''.38$) taken with HST/STIS ($\lambda/\Delta\lambda \sim 5000$, $\lambda = 6000 - 8600 \text{ \AA}$; Ellison et al. 2004), as shown in Ta-

³ This is defined by $\sigma(REW) = \sqrt{\sum_{i=1}^N (\sigma_i \Delta\lambda)^2}$, where N is a number of pixels in the absorption profile, σ_i is the error in the normalized flux at pixel i , and $\Delta\lambda$ is the width of each pixel in angstrom.

⁴ The separation distance between lensed images in the transverse direction is calculated by $D_{\text{tra}} = \theta D_{\text{oa}}$ if $z_{\text{abs}} < z_1$ and $D_{\text{tra}} = \theta \frac{D_{\text{ol}} D_{\text{aq}}}{D_{\text{lq}}} \frac{1+z_1}{1+z_a}$ if $z_{\text{abs}} > z_1$, where θ is an angular separation of the lensed images seen from us, and the subscripts o, a, l, q for D (an angular diameter distance) and z denote observer, absorber, lensing galaxy, and quasar, respectively. We use an average value of z_1 and z_2 for z_a .

ble 1.

To avoid any possible biases for statistical analysis, we accept only absorption lines that satisfy all the following criteria: a) they are blueshifted more than 5000 km s^{-1} from quasar emission redshifts to avoid a contamination by absorption lines that are physically associated to the background quasars, b) they have line widths smaller than the criterion for broad absorption lines (i.e., 2000 km s^{-1}) because of the same reason as above, c) they are not heavily blended with other unrelated absorption lines, d) their equivalent width is larger than 3 times of the noise level (i.e., $REW \geq 3\sigma(REW)$) in spectra⁵, and e) their equivalent width is smaller than 2 \AA to avoid a Damped Ly α (DLA) system whose origin should be different from the CGM. In Table 2, absorption lines with footnote correspond to rejected ones. After the above selection, our sample contains 268 metal absorption lines, of which 96 are from our spectra (68 from Gemini/GMOS and 28 from Keck/ESI spectra), 71 from Ellison et al. (2004), 60 from Monier et al. (1998), and 41 from Smette et al. (1995).

Although our study using gravitationally lensed quasars is a unique and powerful technique to investigate the internal structure of the CGM, there are several caveats. For example, in the CGM, a radial gradient of physical parameter from the center of the gravitational potential of the galaxy hosting the absorption systems cannot be investigated because the host galaxies are not identified. Our sample is also somewhat heterogeneous in terms of spectral resolution and data quality. We will discuss these later in §4.2.

3. RESULTS

We classify all absorption lines into two groups; two-on (2on) and one-on (1on) samples based on line detection with $\geq 3\sigma(REW)$ level in both or one of two spectra of lensed images within 400 km s^{-1} from each other. We also divide absorption lines into three classes based on their ionization potential (IP): high-ions with $IP > 40 \text{ eV}$ (e.g., N v, C iv, and Si iv), low-ions with $IP < 20 \text{ eV}$ (e.g., Al ii, Ni ii, Si ii, Fe ii, Mn ii, Mg ii, N i, O i, Ca ii, and Mg i), and intermediate ones ($20 \text{ eV} \leq IP \leq 40 \text{ eV}$; e.g., Si iii, Al iii, and C ii). As a result, we separate 63 high-ions into 59 2on and 4 1on samples, and 99 low-ions into 72 2on and 27 1on samples, respectively. The rest of them are absorption lines of intermediately ionized ions. All high/low-ionized absorption lines within 400 km s^{-1} are grouped into the “single” absorption system, but most of them have velocity distributions smaller than 100 km s^{-1} .

Figure 1 shows distributions of the physical distance in the transverse direction (D_{tra}) between the sightlines for high-ion and low-ion ionization absorbers as a function of absorption redshift. Thick black curve denotes a physical distance between the sightlines corresponding to the typical lensed quasar from SQLS ($z_{\text{em}} = 2.3$, $z_1 = 0.5$, and $\theta = 2''.0$). For high-ions, our Gemini/GMOS and Keck/ESI spectra sample absorbers with $D_{\text{tra}} \sim 0.1 - 1 \text{ kpc}$ at $z_{\text{abs}} \sim 1.5 - 2.5$. Ellison et al. (2004)

⁵ This is a significance level in absorption strength (i.e., equivalent width), while we detected above all absorption lines (regardless of absorption strength) based on their absorption depth ($> 5\sigma$) at the line center.

TABLE 2
DETECTED ABSORPTION LINES

Lensed QSO	ion	z_1	REW_1 (Å)	$\sigma(REW_1)$ (Å)	z_2	REW_2 (Å)	$\sigma(REW_2)$ (Å)	D_{tra} (pkpc)	dEW	$\sigma(\text{dEW})$
(1)	(2)	(3)	(4)	(5)	(6)	(7)	(8)	(9)	(10)	(11)
SDSS J024634.11−082536.2	Mg II 2800	0.7246	0.692	0.041	0.7256	0.978	0.068	7.86	0.292	0.064
	Mg I 2853	0.7242	0.284	0.037	0.7242	0.774	0.062	7.87	0.632	0.056
	Mg II 2800	1.1218	0.357	0.025	1.1221	0.278	0.050	3.33	0.221	0.151
	Mg II 2800	1.1568	0.837	0.029	1.1572	0.897	0.051	3.04	0.066	0.062
	Mg II 2800	1.3534	0.818	0.025	1.3534	0.774	0.044	1.66	0.053	0.061
	C IV 1550 ^a	1.6892	0.128	0.018	—	<0.077	—	—	>0.399	—
	C IV 1550 ^a	1.7323	0.432	0.024	1.7325	0.438	0.037	—	0.013	0.101
SDSS J074653.03+440351.3	Mg II 2800	1.6505	0.442	0.036	—	<0.116	—	0.642	>0.738	—
	C IV 1550	1.9342	0.700	0.053	1.9342	0.920	0.046	0.099	0.239	0.069
SDSS J080623.70+200631.9	Fe II 2600	0.5736	1.530	0.123	0.5743	2.291	0.271	9.729	0.332	0.095
	Mg II 2800	0.5735	6.398	0.163	0.5741	5.783	0.186	9.731	0.096	0.037
	Ca II 3935	0.5735	0.787	0.059	0.5739	1.021	0.072	9.733	0.229	0.079
	Mg II 2800	—	<0.158	—	0.5516	2.139	0.114	3.242	>0.926	—
SDSS J090404.15+151254.5	Fe II 2600	1.2169	0.964	0.035	1.2170	0.557	0.065	0.886	0.422	0.071
	Mg II 2800	1.2170	3.850	0.035	1.2169	2.452	0.070	0.886	0.363	0.019
	Mg I 2853	1.2166	0.221	0.024	—	<0.157	—	0.887	>0.287	—
	C IV 1550	1.6130	1.041	0.049	1.6127	0.769	0.117	0.237	0.261	0.118
	Mg II 2800	1.6125	0.434	0.025	1.6126	0.451	0.057	0.237	0.0374	0.134
	C IV 1550	1.6547	1.175	0.045	1.6540	1.039	0.104	0.186	0.116	0.094
	Al II 1670	1.6530	0.142	0.023	1.6499	0.218	0.057	0.189	0.346	0.202
	Mg II 2800	1.6523	0.605	0.024	1.6526	0.268	0.048	0.188	0.557	0.081
	C IV 1550	1.7686	0.457	0.032	1.7707	0.323	0.078	0.057	0.294	0.179
SDSS J092455.87+021924.9	Mg II 2800	—	<0.071	—	1.0785	0.245	0.042	1.341	>0.709	—
SDSS J100128.61+502756.8	Mg II 2800	—	<0.358	—	0.4145	1.893	0.206	15.700	>0.811	—
	Fe II 2600	0.8723	0.606	0.021	0.8720	0.478	0.036	7.794	0.211	0.066
	Mg II 2800	0.8718	2.045	0.068	0.8717	1.758	0.091	7.799	0.140	0.053
	Mg I 2853	0.8720	0.235	0.045	0.8719	0.219	0.058	7.797	0.068	0.303
	Si II 1526	1.6066	0.172	0.044	1.6065	0.275	0.058	1.103	0.372	0.208
	C IV 1550	1.6074	2.400	0.062	1.6071	2.194	0.113	1.100	0.086	0.053
	Al III 1854	1.6077	0.178	0.018	1.6075	0.218	0.027	1.098	0.181	0.131
	Fe II 2600	1.6072	0.352	0.019	1.6071	0.379	0.019	1.100	0.072	0.068
	Mg II 2800	1.6074	1.559	0.023	1.6073	1.363	0.028	1.099	0.126	0.022
	Mg I 2853	1.6072	0.193	0.020	1.6071	0.225	0.015	1.100	0.142	0.103
	C IV 1550	1.7542	0.644	0.041	1.7563	0.421	0.064	0.368	0.347	0.108
	Si IV 1393 ^b	1.7711	0.856	0.083	1.7704	1.029	0.152	0.299	0.168	0.148
	C IV 1550 ^b	1.7748	5.201	0.064	1.7742	1.738	0.078	0.282	0.666	0.016
	C IV 1550 ^c	1.8151	1.508	0.035	1.8147	1.076	0.046	0.108	0.286	0.035
SDSS J113157.72+191527.7	Fe II 2600	1.1902	0.944	0.034	1.1902	1.719	0.098	1.923	0.451	0.037
	Mg II 2800	1.1902	2.841	0.028	1.1902	4.577	0.080	1.924	0.379	0.012
	Mg I 2853	1.1902	0.082	0.017	1.1899	0.522	0.059	1.924	0.842	0.038
	Fe II 2600	1.4215	1.958	0.026	1.4191	2.597	0.092	1.416	0.246	0.029
	Mg II 2800	1.4202	6.484	0.030	1.4190	5.753	0.105	1.418	0.113	0.017
	Mg I 2853	1.4215	0.472	0.024	1.4189	0.707	0.081	1.416	0.333	0.084
	Mg II 2800	1.5615	0.578	0.027	—	<0.246	—	1.168	>0.574	—
	Mg II 2800	1.7943	0.965	0.030	—	<0.301	—	0.837	>0.688	—
	C IV 1550	1.8474	1.361	0.058	1.8475	1.298	0.066	1.103	0.047	0.063
	Si IV 1393	1.9957	1.096	0.086	1.9960	1.112	0.090	0.837	0.015	0.111
SDSS J125819.24+165717.6	C IV 1550	1.9973	1.159	0.053	1.9989	1.374	0.064	0.833	0.156	0.055
	C IV 1550	2.1062	1.019	0.047	2.1066	0.855	0.056	0.664	0.161	0.067
	Si IV 1393	2.2501	0.198	0.028	2.2505	0.147	0.024	0.466	0.259	0.158
	C IV 1550	2.2500	0.555	0.092	2.2500	0.358	0.110	0.466	0.355	0.224
	Si IV 1393	2.3868	0.631	0.045	2.3865	0.813	0.064	0.304	0.223	0.082
	C IV 1550	2.3848	0.521	0.066	2.3852	0.783	0.078	0.305	0.335	0.107
	Al II 1670	2.3842	0.344	0.036	2.3846	0.407	0.036	0.306	0.154	0.116
	Fe II 2600	2.3840	0.428	0.036	2.3843	0.472	0.037	0.306	0.093	0.104
SDSS J134929.84+122706.8	Mg II 2800	0.4913	0.936	0.083	—	<0.622	—	18.141	>0.336	—
	Mn II 2576	—	<0.050	—	1.2395	0.213	0.035	5.780	>0.765	—
	Fe II 2600	1.2374	1.559	0.032	1.2376	1.974	0.070	5.812	0.210	0.032
	Mg II 2800	1.2373	3.383	0.035	1.2375	4.456	0.071	5.814	0.241	0.014
	Mg I 2853	1.2373	0.546	0.027	1.2375	0.817	0.058	5.814	0.332	0.058
SDSS J135306.35+113804.7	Mg II 2800	0.6377	1.032	0.052	0.6378	0.982	0.025	2.663	0.049	0.058
	Fe II 2600	0.9047	0.773	0.022	0.9048	1.263	0.009	1.537	0.387	0.018
	Mg II 2800 ^d	0.9047	2.300	0.033	0.9048	3.460	0.017	1.537	0.335	0.010
	Mg I 2853	0.9045	0.317	0.015	0.9048	0.292	0.045	1.538	0.080	0.149
	Fe II 2600	1.2386	0.204	0.022	1.2389	0.103	0.012	0.636	0.493	0.079
	Mg II 2800	1.2387	0.983	0.026	1.2385	0.941	0.017	0.636	0.042	0.031
	C IV 1550	—	<0.534	—	1.5689	0.978	0.062	0.073	>0.454	—

^a Absorption redshift is larger than the quasar emission redshift.

^b Broad Absorption Line (BAL) with a FWHM $\geq 2000 \text{ km s}^{-1}$.

^c Velocity shift from the quasar emission redshift is smaller than 5000 km s^{-1} .

^d This line is blended with other physically unrelated lines.

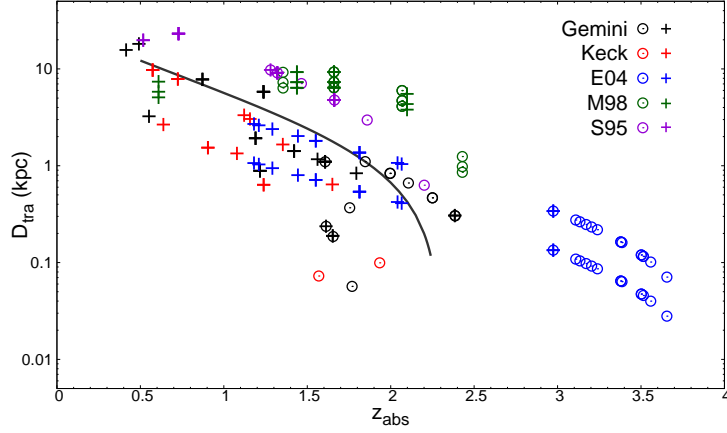


FIG. 1.— Physical distance between sightlines of lensed images (D_{tra}) as a function of absorption redshift (z_{abs}). Data from our sample are shown with black (Gemini/GMOS) and red (Keck/ESI), while those from the literature are shown with blue (Ellison et al. 2004), green (Monier et al. 1998), and purple (Smette et al. 1995). open circles and crosses denote high-ion and low-ion absorption lines, respectively. Strong absorption lines with $REW > 2 \text{ \AA}$ are also included in the figure. Thick black curve denotes a physical distance between the sightlines corresponding to the typical lensed quasar from SQLS ($z_{\text{em}} = 2.3$, $z_1 = 0.5$, and $\theta = 2''0$).

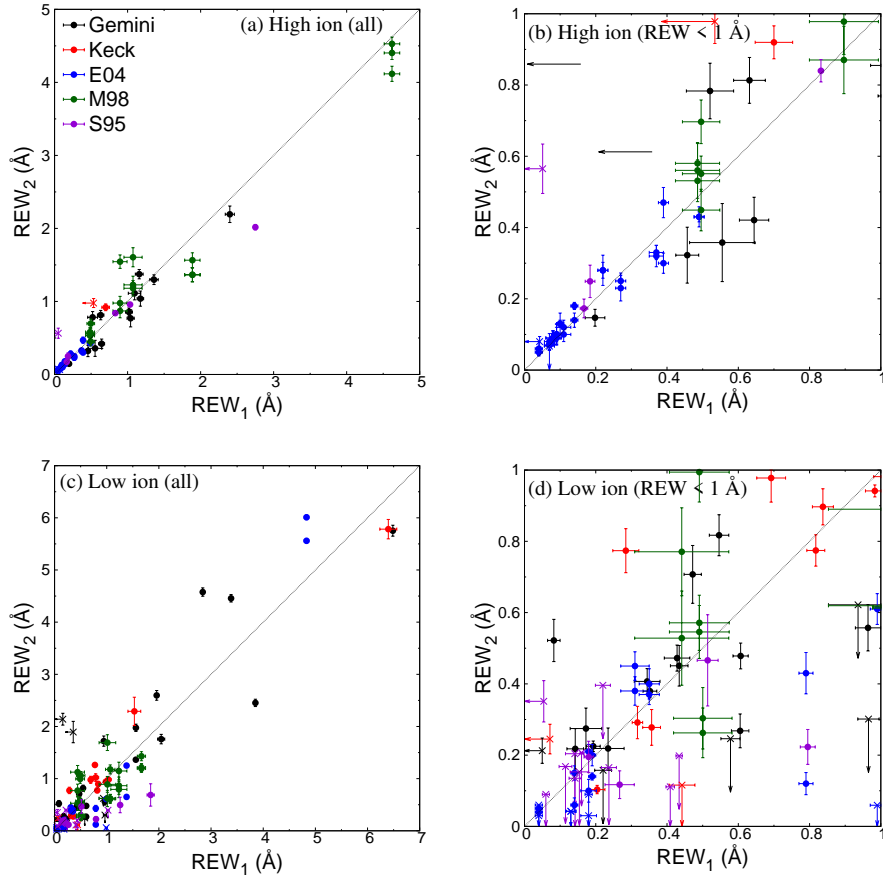


FIG. 2.— Correlation between rest-frame equivalent widths (REW s) of absorption lines detected along both or one of the two sightlines. Upper panels show distributions of all high-ion absorption lines (a) and its close-up view up to $REW = 1 \text{ \AA}$ (b). The corresponding plots for low-ion absorption lines are shown in lower panels (c,d). The meaning of symbol colors are same as Figure 1. For low-ion absorbers, only upper limits are shown with arrows. If data points locate on the dashed lines, the observed REW in one sightline is equal to that in another sightline.

sample absorbers at higher redshift up to $z_{\text{abs}} \sim 3.6$, while Monier et al. (1998) and Smette et al. (1995) sample those with larger physical distance up to $D_{\text{tra}} \sim 10$ kpc. On the other hand, for low-ions all data source sample absorbers with $D_{\text{tra}} \sim 0.1 - 10$ kpc at $z_{\text{abs}} \sim 0.5 - 2.0$, although Ellison et al. (2004) have several sample at higher redshift up to $z_{\text{abs}} \sim 3$. By combining our high ion samples (black and red open circles in Figure 1) with that of Ellison et al. (2004) (blue open circles in Figure 1), we can examine the redshift evolution of absorbers with a scale of $D_{\text{tra}} \sim 0.1 - 1$ kpc. On the other hand, we can examine physical properties of absorbers with a wide range of distance in $D_{\text{tra}} \sim 0.1 - 10$ kpc at $z_{\text{abs}} \sim 2$.

We first compare strengths of absorption lines (i.e., REW) in the two sightlines as shown in Figure 2 for high and low-ions. Samples from Ellison et al. (2004) and Smette et al. (1995) tend to have smaller REW s, while those from Monier et al. (1998) and our sample have larger values. This is because the former are detected in spectra with higher S/N ratio (i.e., due to a technical reason). Correlation coefficients between REW s along sightline pairs are almost same; $r = 0.981$ and $r = 0.933$ for high-ions and low-ions, respectively (see Figure 2 (a) and (c)). However, we find larger scatter for low-ions ($r = 0.594$) compared to high-ions ($r = 0.941$) if we consider only weak absorption lines with REW smaller than 1.0 \AA , as noted in Ellison et al. (2004) (see Figure 2 (b) and (d)). This could be due to a clustering effect. If strong/weak absorption lines correspond to regions with high/low number density of gas clouds, only the weaker ones with a sparse cloud distribution are affected by a typical scale of each cloud that should be smaller for low-ionized absorbers.

Thus, a typical scale of absorbers probably depends on their ionization condition; those in higher ionization condition tend to have larger size (e.g., Stern et al. 2016). Therefore, we investigate the fractional equivalent width difference dEW as a function of transverse distance between sightlines as shown in Figure 3. Because most absorption systems in our sample are detected at redshift higher than those of lensing galaxies (i.e., $z_{\text{abs}} > z_l$), the corresponding physical separation between sightlines becomes larger at lower redshift. Therefore, low-ions such as Mg II and Fe II, whose rest-frame wavelengths are larger than those of high-ions like C IV and Si IV, are detected at lower redshifts and we can perform multiple sightline spectroscopy only for larger separation distances.

We then compare the dEW distributions as a function of D_{tra} after separating D_{tra} into three bins for high- and low-ion samples in such a way that each bin contains almost same number of absorption lines. Because we confirmed that dEW distribution is not Gaussian, we regard the range between 30 percentile and 70 percentile of the dEW distribution in each bin as a core distribution range of dEW (dEW box, hereafter; see Figure 3). The dEW box for high ions are $0.10 - 0.20$, $0.10 - 0.26$, and $0.08 - 0.17$ in D_{tra} of $0.02 - 0.2$, $0.2 - 2.0$, and $2.0 - 10.0$ kpc, while the dEW box for low ions are $0.13 - 0.42$, $0.07 - 0.33$, and $0.17 - 0.42$ in D_{tra} of $0.1 - 1.0$, $1.0 - 3.0$, and $3.0 - 20$ kpc, respectively. We confirm that the dEW distributions are almost independent of D_{tra} for

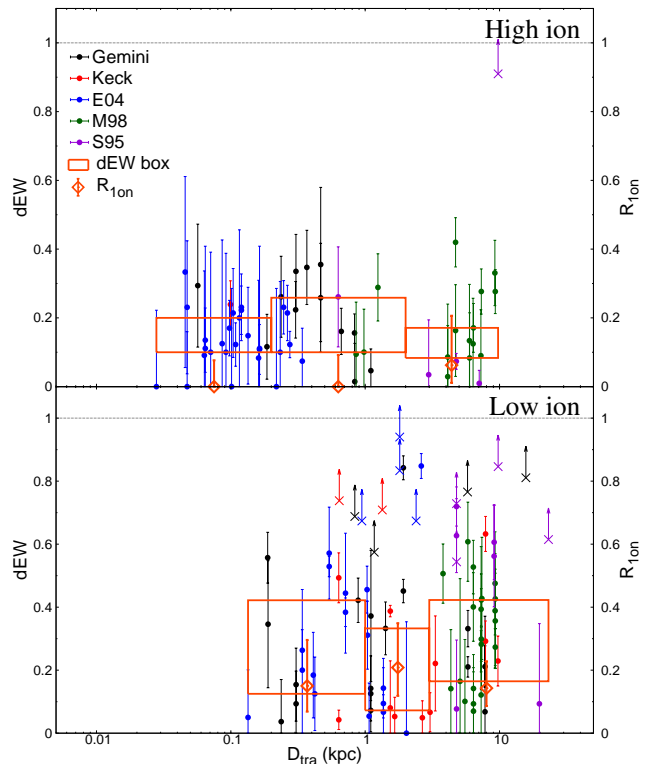


FIG. 3.— Fractional equivalent width (dEW) and 1on ratio (R_{1on}) for high (top) and low (bottom) ions as a function of sightline separation (D_{tra}). The meaning of symbol colors are same as Figures 1 and 2. If absorption lines are 1on sample, only lower limits of dEW are plotted with upward arrows. The range of 30 – 70 percentile of dEW distribution (dEW box) and 1on ratio (R_{1on}) are shown with orange rectangles and open diamonds after separating D_{tra} range into three bins.

both of high and low ion samples ($dEW \sim 0.2$) although the low-ion sample has a slightly larger variation. We also do not find any remarkable redshift evolution of the dEW distribution for high-ion absorbers in the range of $D_{\text{tra}} \sim 0.1 - 1$ kpc, comparing our sample at $z_{\text{abs}} \sim 2$ (black and red filled circles in Figure 3) and those from Ellison et al. (2004) at $z_{\text{abs}} \sim 3.3$ (blue filled circles in Figure 3).

We also compare the fraction of 1on lines (1on ratio, hereafter) defined by

$$R_{1on} = \frac{N_{1on}}{N_{2on} + N_{1on}}, \quad (2)$$

where N_{1on} and N_{2on} are numbers of 1on and 2on lines. Because the R_{1on} value strongly depends on the quality of spectra (i.e., detection limit), we calculate the ratio using only reliable 1on lines; 3σ detection limit on REW in an undetected sightline is smaller than 50% of REW in a detected sightline (i.e., $6\sigma(REW_{\text{undet}}) < REW_{\text{det}}$)⁶ to find larger values for low-ions ($R_{1on} \sim 0.16$) than high-ions ($R_{1on} \sim 0.02$). This result suggests that a typical scale of low-ion absorbers is smaller than those of high-ion absorbers, which is consistent with the results from the past studies (e.g., Ellison et al. 2004; Stern et al. 2016) and the correlation analysis for weak absorption lines

⁶ REW_{det} is a rest-frame equivalent width in spectra of detected sightline, while $\sigma(REW_{\text{undet}})$ is a 1σ detection limit on REW in spectra of undetected sightline.

(Figure 2 (b) and (d)).

4. DISCUSSION

In previous section, we discovered several properties on dEW and R_{1on} for high and low-ion absorbers. In order to connect our findings with the internal structure of the CGM that cannot directly be observed, we construct simple models to reproduce the observed properties. We assume a two-component model for the CGM; a number of spherical gas clouds are embedded in diffusely distributed gas and both of them give rise to the metal absorption lines. Although the ionization state depends on several parameters including electron density, photon density, and gas temperature, we assume a single ionization state for each of the two-components, for simplicity. The EW s of both components are summed to measure a total EW , although only spherical clouds have a radial gradient of EW . Thus, the total equivalent width depends on a) an equivalent width distribution as a function of radius r from the center of each spherical cloud ($EW(r)$) and b) an intensity of equivalent width by diffusely distributed gas component (EW_{diff}). Focusing on the probability that the spherical clouds and the diffuse component locate along the two sightlines toward the background quasars, the cross section of the absorbers depends on their sizes. Here, we also define c) a size (diameter) of each spherical cloud (d) and d) an overall size of diffuse component (L). Here, for simplicity, we assume that a number of spherical clouds randomly distribute on scale of L in a square region⁷. The covering factor of the absorbing clouds also determines the incidence rate of the clouds. In this model, we define e) a covering factor of clouds (C_f). Using the five parameters above (i.e., $EW(r)$, EW_{diff} , d , L , and C_f), we examine the incidence rate of gas clouds and the total equivalent width in the two sightlines toward the background quasars. Because high and low-ion absorption lines are not necessarily arising at the same gas, we make models for each of them, respectively. In the above model, we use the equivalent width distribution instead of the column density distribution because equivalent widths can be compared to the observation directly.⁸ First, we place a number of spherical clouds in a square field with a 10 kpc margin (that correspond to the maximum separation distance of our sample) around the square field (see left panel of Figure 4). And then, we divide sightline distance into 6 bins, randomly choose 1000 sightline pairs for each bin (i.e., 6000 random sightline in total), and measure equivalent widths for them (EW_1 and EW_2). We repeat such measurements for each model by changing five parameters above to find the best model to reproduce the observations (see Figure 5 and Table 3).

Among several free parameters, we first consider physical acceptable functions for the radial distribution of the equivalent width. In this paper, we assume three simple $EW(r)$ functions described below.

(a) Elliptical function:

⁷ Because models with clouds in *square* area and *circle* area give almost same results with only a few % difference in dEW and R_{1on} distributions, we adopt the former for our calculation.

⁸ If absorption lines are not saturated (i.e., its central optical depth is $\tau_0 \ll 1$), their equivalent widths are almost proportional to the column density at the linear part of the curve of growth. We can apply this assumption for a substantial fraction of our sample.

TABLE 3
MODEL PARAMETERS

Model	function ^a	d^b (kpc)	L^c (kpc)	EW_{diff}^d	C_f^e
(1)	(2)	(3)	(4)	(5)	(6)
A	ell.	1	50	...	1
B	inv.	1	50	...	1
C	lin.	1	50	...	1
D	ell.	0.5	50	...	1
E	ell.	5	50	...	1
F	ell.	10	50	...	1
G	ell.	1	100	...	1
H	ell.	1	500	...	1
I	ell.	1	50	0.01	1
J	ell.	1	50	0.05	1
K	ell.	1	50	0.1	1
L	ell.	1	50	0.5	1
M	inv.	1	50	0.01	1
N	inv.	1	50	0.02	1
O	inv.	1	50	0.05	1
P	ell.	1	50	...	2
Q	ell.	1	50	...	1.5
R	ell.	1	50	...	0.5
Best Model 1 (high-ion)	ell.	1	500	...	2
Best Model 2 (high-ion)	ell.	0.5	500	0.5	1
Best Model 3 (low-ion)	ell.	1	500	...	1.5

^a Function of radial distribution of equivalent width: elliptical (ell.), inverse proportional (inv.), and linear (lin.) functions.

^b Size of each absorbing cloud.

^c Overall size of the CGM.

^d Intensity of equivalent width in a diffuse gas.

Three dots means no diffuse gas is added.

^e Covering factor of clouds in the CGM.

If absorbers have a spherical shape with no internal structure (i.e., homogeneous density), an equivalent width is proportional to a projected depth of the absorber unless an absorbing cloud is optically thick. In this case, the equivalent width distribution is expressed by

$$EW(r) = EW_{\max} \sqrt{1 - \frac{r^2}{(d/2)^2}}, \quad (3)$$

where r is the distance from the center of each spherical cloud, d is a diameter of the cloud, and EW_{\max} is an intensity of equivalent width at $r = 0$.

(b) Inverse proportional function:

Another possible model is a singular isothermal sphere with the radial density distribution of $\rho(r) \propto r^{-2}$. In this model, a projected density (i.e., column density) at a distance from the center r is approximately expressed by an inverse proportional function except for at very large radius. To avoid it from diverge to infinity at the center, we slightly change the function into

$$EW(r) = \frac{EW_{\max} \left(\frac{EW_{\min}}{EW_{\max} - EW_{\min}} \frac{d}{2} \right)}{\left(r + \frac{EW_{\min}}{EW_{\max} - EW_{\min}} \frac{d}{2} \right)}, \quad (4)$$

where EW_{\min} is the minimum observational value of EW in our sample.

(c) Linear function:

For comparison to the results from models adopting

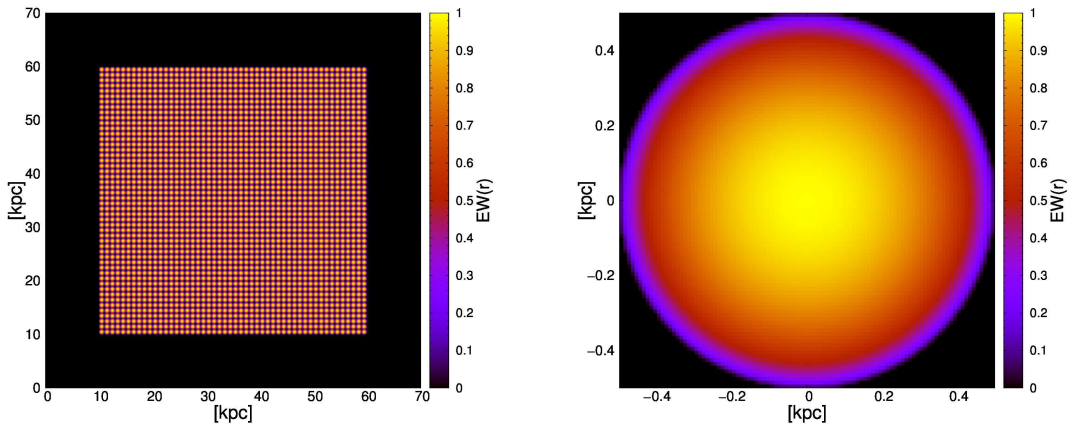


FIG. 4.— Sample model of the CGM with a default parameters: an elliptical function, a size of each spherical cloud of $d = 1$ kpc, an overall size of the CGM of $L = 50$ kpc, a covering factor of $C_f = 1$ with no intensity of equivalent width by diffuse gas ($EW_{\text{diff}} = 0$). Left and right panels show a whole range of the modeled CGM and its close-up of a cloud.

the above equivalent width distributions, we also examine a simple model expressed by

$$EW(r) = -\frac{EW_{\text{max}}}{(d/2)}r + EW_{\text{max}}. \quad (5)$$

We adopt a dimensionless number to set $EW_{\text{max}} = 1$ as the maximum equivalent width at the center, because we only measure the fractional equivalent width difference (dEW) (i.e., the amplitudes of EW_{max} and EW_{min} themselves do not necessarily have to be measured.). We also regard sightlines with equivalent widths greater than $EW_{\text{min}} = 0.01$ as absorption-detected sightlines because the ratio of the maximum and the minimum REWs in our observed sample is ~ 100 . The radial distribution functions for an equivalent width depend mainly on the dEW distribution as a function of D_{tra} . As shown in Figure 5 (a), the elliptical and the inverse proportional functions show almost same patterns of dEW and $R_{1\text{on}}$ distributions as a function of D_{tra} that well match to the observed trends (i.e., the dEW box is ~ 0.2 and almost independent of D_{tra} .) although $R_{1\text{on}}$ is rather over-estimated. Among the two acceptable functions, we will use the elliptical function as our default model. As for the other parameters, we use $d = 1$ kpc⁹, $L = 50$ kpc¹⁰, and $C_f = 1$ with no diffusely distributed homogeneous gas ($EW_{\text{diff}} = 0$) as default parameters.

Next, we consider models with different sizes of each spherical cloud, $d = 0.5, 1, 5$, and 10 kpc using defaults values for all the other parameters. It is clear that both dEW and $R_{1\text{on}}$ start to rise at smaller D_{tra} for models with smaller cloud size (see Figure 5 (b)). We also change an overall size L from $50, 100$, to 500 kpc. As shown in Figure 5 (c), any clear differences are not seen in the

dEW distribution. On the other hand, $R_{1\text{on}}$ tends to have larger values at $D_{\text{tra}} \geq 1$ kpc especially for models with smaller overall size. This is because a number of 1on pairs that locate at the edge of overall area increase for those models.

In addition to the clumpy spherical gas clouds, the CGM could have a diffusely distributed homogeneous gas whose ionization condition is higher than that of the spherical clouds because of lower gas density. We add such a component (we call this *diffuse gas*, hereafter) whose equivalent width is 10% of the central value (i.e., $EW_{\text{diff}} = 0.1$) throughout the overall area. Once the diffuse gas is added, 1on pairs are seen only at the edge of overall area, which decreases $R_{1\text{on}}$ significantly as shown in Figure 5 (d). We also consider models with four diffuse gas intensities with $EW_{\text{diff}} = 0.01, 0.05, 0.1$, and 0.5 for the elliptical function and $EW_{\text{diff}} = 0.01, 0.02$, and 0.05 for the inverse proportional function. Although both functions have acceptable models, their diffuse gas intensities are very different; best models have diffuse gas intensity of $EW_{\text{diff}} = 0.5$ and 0.01 for the elliptical and the inverse proportional functions, respectively (Figure 5 (e) and (f)).

Lastly, we consider the covering factor C_f , which is the fraction of the overall area that is covered by a number of spherical clouds, in Figure 5 (g). Here, we regard $C_f = 1$ if clumpy clouds are regularly arranged with no gaps between clouds although there are cracks¹¹ in the diagonal directions (see Figure 4). If we decrease the covering factor down to 0.5 , $R_{1\text{on}}$ increases significantly to become inconsistent with the observation (Figure 5 (g)). Therefore, we also attempt to increase C_f to 1.5 and 2 that means 50% or 100% of the cracks are covered by other foreground/background clouds along our sightlines. As show in Figure 5 (d) and (g), the $R_{1\text{on}}$ distributions of the model with the $C_f = 2$ (Model P in Table 3) and the

⁹ This is a typical size of N II absorbers whose ionization parameter IP = 29.6 eV is between those of C IV (64.5 eV) and Mg II (15.0 eV) (Stern et al. 2016)

¹⁰ This is large enough (five times larger) compare to the maximum scale of our observation, ~ 10 kpc

¹¹ Gaps between spherical clouds seen from us, toward which the corresponding equivalent width is zero.

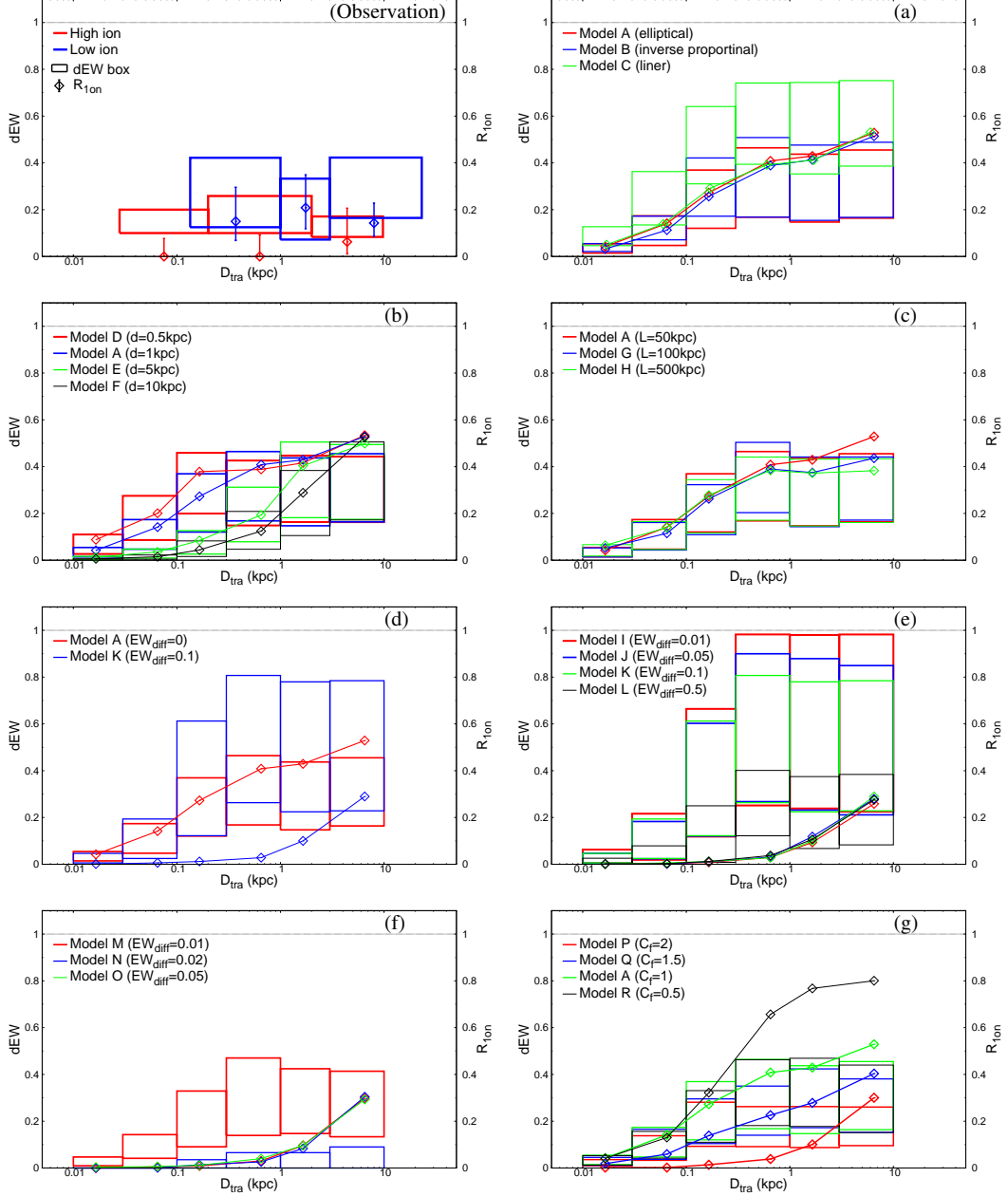


FIG. 5.— Same as Figure 3, but for models. The range of 30 – 70 percentile of dEW distribution and 10n ratio are shown with rectangles and open diamonds. We adopt default condition (Model A in Table 3): spherical clouds with a size of $d = 1$ kpc, whose radial distribution of equivalent width ($EW(r)$) is written by an elliptical function, a covering factor of $C_f = 1$ with no intensity of equivalent width by diffuse gas ($EW_{\text{diff}} = 0$) in a square region (i.e., CGM) with a length of one side of $L = 50$ kpc. Results are shown for models if we change a function of radial distribution of equivalent width (a), a size of each spherical cloud (b), an overall size of the CGM (c), an addition of diffuse gas (d), a strength of diffuse gas for both functions (e,f), and a covering factor (g). See Table 3 for adopted parameters in detail.

model with the diffuse gas (e.g., Model K in Table 3) are very similar to each other. Because there are no cracks inside the CGM in both the models, 10n sample occurs only at the edge of the modeled CGM.

4.1. Optimized Models

After repeating above models by changing five parameters, we select the best models for high and low-ion samples respectively, as shown in Figure 6 whose best parameters are summarized in Table 3. We chose the best models based on the following two criteria; 1) R_{10n} values from the model and the observation are consistent to each other within 1σ errors for a wide range of D_{tra} ,

and 2) the model and the observation have the largest common areas of dEW boxes among those satisfying the first criterion. As summarized below, our best models suggest both high and low-ion absorbers have large (or full) coverage fraction along our sightlines. However, the coverage fraction (i.e., a volume number density of gas clouds) should be inversely proportional to the distance from host galaxies (e.g., Rudie et al. 2012), while we assume a constant cloud density throughout the CGM. Our observation can be biased for regions in the vicinity of host galaxies (e.g., ≤ 100 kpc) where the coverage fraction is probably very high.

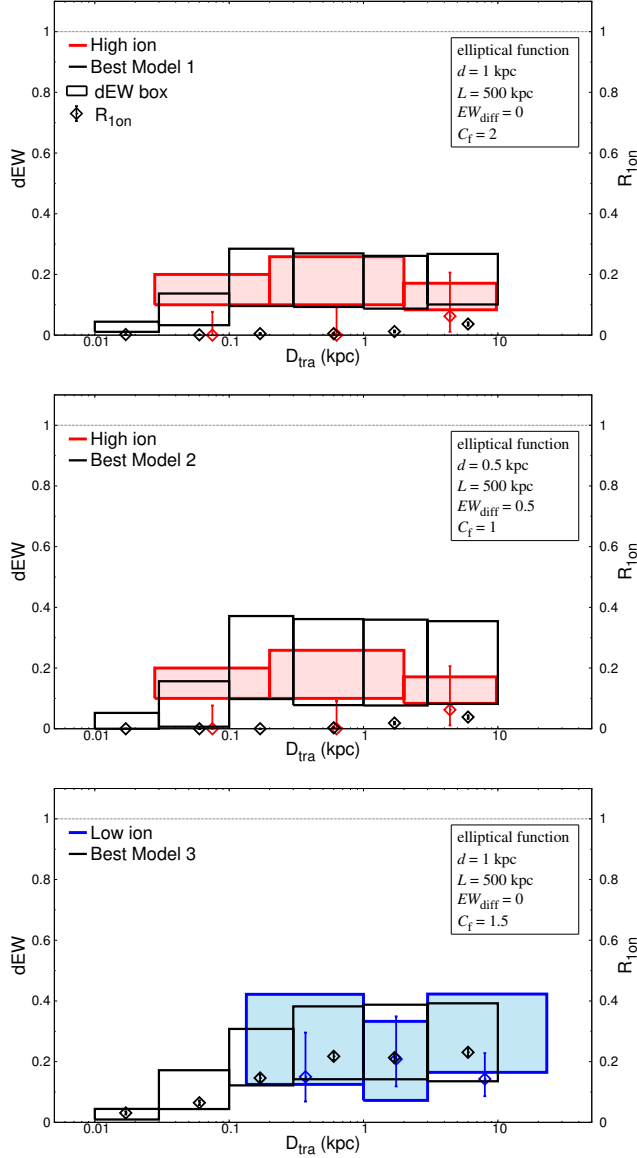


FIG. 6.— Same as Figure 5, but for the best models for high-ions (top and middle) and low-ions (bottom). A colored rectangles and open diamonds indicates observed values, while a black ones indicate the model values. The best parameters for high-ions are elliptical function, $d = 1$ kpc, $L = 500$ kpc, $C_f = 2$, with no intensity of EW by diffuse gas (top panel) or elliptical function, $d = 0.5$ kpc, $L = 500$ kpc, $C_f = 1$, with an intensity of $EW_{\text{diff}} = 0.5$ (middle panel). The best parameters for low-ions are elliptical function, $d = 1$ kpc, $L = 500$ kpc, $C_f = 1.5$, with no diffuse gas (bottom panel).

First, we focus on high ion absorbers. As shown in Figure 3, an average value of the fractional difference of equivalent widths (dEW) is obviously larger than ~ 0.1 at the scale of $D_{\text{tra}} \sim 0.1$ kpc, which means that there exist small-size clouds or density fluctuations at the corresponding scale. As shown in Figure 5 (b), the size of each cloud should be smaller than ~ 1 kpc. Otherwise, dEW is under-estimated at $D_{\text{tra}} \sim 0.1$ kpc. The $10n$ ratio (R_{10n}) leaves zero only at larger scales of several kilo-parsecs, which requires us to choose an overall size of the CGM larger than $L \sim 100$ kpc (see Figure 7) once we adopt the best value for a covering factor ($C_f = 2$) later. It is probably comparable to or larger

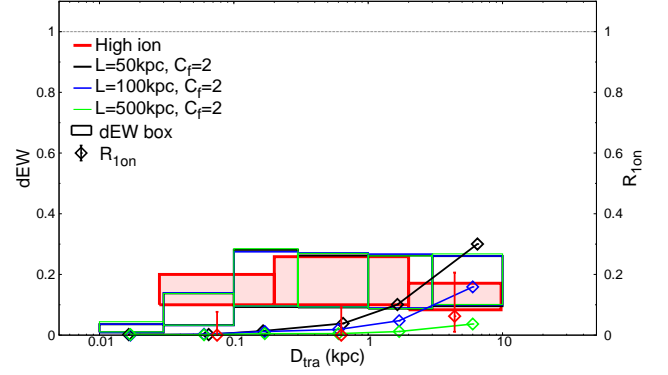


FIG. 7.— Same as Figure 5 (c), but using the best value for a covering factor ($C_f = 2$) instead of the default value ($C_f = 1$). The observed results for high-ions are also overlaid.

than the overall size for low-ion absorber ($L > 500$ kpc as described below) because high-ionized absorbers usually have a larger distribution than low-ionized absorbers (e.g., Stern et al. 2016). High-ion absorbers cannot have any small-scale cracks therein because their R_{10n} is zero at D_{tra} smaller than several kilo-parsec. Based on the above considerations, we find two best models for high-ion absorbers. They have an overall size of ~ 500 kpc or more with clumpy clouds (or density fluctuation) smaller than 1 kpc whose equivalent widths distribution follows the elliptical function¹². They have no cracks between small clouds, which can be reproduced by either $C_f = 2$ or a diffuse gas with an intensity of $EW_{\text{diff}} = 0.5$ (Figure 6 and Table 3). Here, we emphasize that the best size of each cloud is $d \leq 0.5$ kpc (instead of ≤ 1 kpc) in the latter case. Thus, we infer that high-ion absorbers originate in a widely distributed homogeneous gas with a scale of ≥ 500 kpc, in which there exists a small scale ($\leq 0.5 - 1$ kpc) fluctuation of equivalent width. Compared to our best model, the past results for the CGM at $z < 0.1$ suggested they have a smaller overall size of $\sim 100 - 200$ kpc around galaxies (Chen et al. 2001; Bordoloi et al. 2014; Burchett et al. 2016). As to covering factor, Chen et al. (2001) got a similar result to ours (i.e., full coverage) within ≤ 100 kpc from host galaxies, although a partial coverage was sometimes suggested even at smaller impact parameters (e.g., Bordoloi et al. 2014). The detection rate of C IV absorption lines also depends on star-formation rate and stellar mass of host galaxies as well as a Mpc scale galaxy number density around host galaxies.

For low-ion absorbers, dEW is almost flat at $D_{\text{tra}} \sim 0.1 - 10$ kpc like high-ion absorbers. Such distributions can only be reproduced by small clumpy clouds with scales smaller than $d \leq 1$ kpc (see Figure 5 (b)). The $10n$ ratio is also flat at the same D_{tra} range, which requires an overall size greater than $L \sim 500$ kpc. Covering factor (C_f) should be larger than 1 (to avoid an over-estimation of R_{10n}) but smaller than 2 (to make sub-kpc scale gaps so that R_{10n} is not zero). Our best model for low-ion absorbers has an overall size of ~ 500 kpc or more with small clumpy clouds (or fluctuation) with a scale of ~ 1 kpc. These are same as those for high-ion absorbers. However, their covering factor is smaller ($C_f =$

¹² The model using the inverse proportional function is also acceptable, but the elliptical function gives a better result.

1.5) than high-ion absorbers ($C_f = 2$), which means that low-ion absorbers have cracks with a scale of ≤ 1 kpc (see Figure 6 and Table 3). This is why only low-ion absorbers have a substantial 1on ratio as small as $D_{\text{tra}} \sim 0.1$ kpc. For the same reason, low-ion absorbers do not have a homogeneous gas component (i.e., $EW_{\text{diff}} = 0$). Therefore, we expect that a low-ion absorber consists of a large number of clumpy dense clouds with a scale of ≤ 1 kpc. Again, the past results predicted a smaller size of the CGM (~ 200 kpc; Nielsen et al. e.g., 2013; Churchill et al. e.g., 2013) based on Mg II absorption lines at $z < 1$, compared to our best model. The covering factor of Mg II was also estimated as $C_f \sim 0.6 - 0.9$, depending on an azimuthal angle; the higher covering factors along the projected galaxy major and minor axes (Kacprzak et al. 2012).

Thus, the best model above requires three components in total: i.e., clumpy clouds for high-ions, clumpy clouds for low-ions, and diffuse homogeneous gas for high-ions. Obviously, these three components have different ionization conditions. To locate the origins of them, we performed simple calculations using the photoionization code Cloudy, version 17.00 (Ferland et al. 2017), on a slab of gas illuminated with extragalactic background radiation (Haardt & Madau 2012) at $z = 2.0$ (a typical z_{abs} in our sample). We assume a constant metallicity of $\log(Z/Z_{\odot}) = -1.0$ throughout the gas whose total hydrogen column density is $\log N_{\text{H}} = 18.0 \text{ cm}^{-2}$ in the optically thin regime¹³. We varied the ionization parameter ($\log U$) in steps of 0.1 dex from -4.0 to 0.0 (which corresponds to the gas density of $\log n \sim -0.6 - -4.6$ at $z = 2.0$), and then calculated the ionization fractions of C^{3+} (C IV), Mg^{+} (Mg II), and O^{5+} (O VI) (as an example of higher ionized absorbers)¹⁴. As shown in Figure 8, the ionization fractions of Mg^{+} and C^{3+} are dominant at $\log U < -3$ ($\log n > -2$) and $\log U \sim -3 - -1$ ($\log n \sim -2 - -4$) respectively, which are probably optimal for the C IV and Mg II absorbers. On the other hand, at $\log U > -1$ ($\log n < -4$), the fraction of O^{5+} becomes dominant although a substantial fraction of Carbon still remains in C^{3+} . Thus, the O VI absorbers in higher ionization condition that are frequently detected in the CGM (Tumlinson et al. 2011; Turner et al. 2014) could be the origin of the diffusely distributed C IV absorbers, while the spherical components of C IV and Mg II absorbers correspond to the gas whose ionization parameters are optimal for them.

4.2. Caveats

Here, we list some caveats on our results that should be noted:

- The source of absorber (i.e., a host galaxy) was not identified. There are several origins including dwarf galaxy, low surface brightness galaxy, galaxy merger, galaxy outflow, AGN outflow, and so on. Without identifying host galaxies, we cannot narrow down possible sources. Because of the

¹³ At the range of ionization parameter that we modeled ($\log U = -4.0 - 0.0$), a total column density of neutral hydrogen is always smaller than $\log N_{\text{HI}} = 17.2 \text{ cm}^{-2}$.

¹⁴ In this assumption, since the gas temperature is $\sim 4 \times 10^5$ K, collision excitation does not substantially contribute.

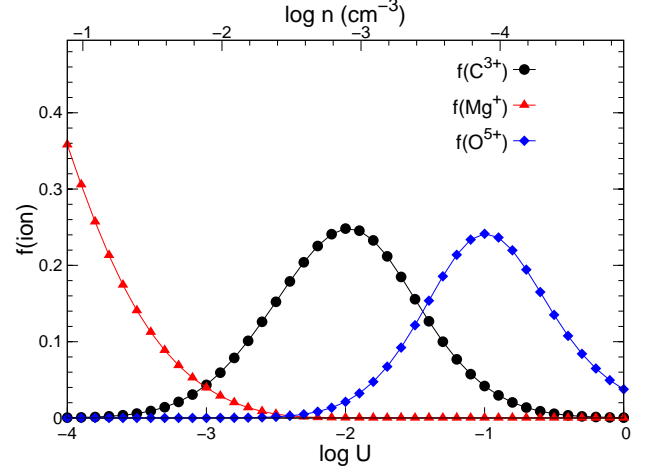


FIG. 8.— Ionization fractions ($f(\text{ion})$) of C^{3+} , Mg^{+} , and O^{5+} as a function of ionization parameter ($\log U$) (bottom label) and a gas volume density ($\log n$) at $z = 2.0$ (top label). Photoionization models are conducted using the code Cloudy (ver. 17.00), assuming a plane-parallel slab that is illuminated with the extragalactic background radiation at $z = 2.0$. We also assume a constant metallicity of $\log(Z/Z_{\odot}) = -1.0$ throughout the gas whose total hydrogen column density is $\log N_{\text{H}} = 18.0 \text{ cm}^{-2}$.

same reason, we did not make a “0on” sample (i.e., no absorption is detected in both sightlines even if there exist a galaxy close to our sightlines to the quasars.) in addition to 1on and 2on samples because we do not know the locations of galaxies close to our sightlines in advance, which could overestimate a covering factor ($C_f \geq 1.5$) and also a size of the CGM ($L \geq 500$ kpc).

- Only five free parameters are obviously not enough to make models. It can be improved by adding radial functions of gas density and volume density of spherical cloud from the center of the CGM as additional free parameters. Indeed, both optical depth and equivalent width of C IV absorption lines at $D_{\text{tra}} \sim 500$ kpc are about one order of magnitude smaller than those at $D_{\text{tra}} \sim 100$ kpc (e.g., Turner et al. 2014; Turner 2015). The CGM absorption strength also depends on physical properties of host galaxies such as luminosity, star formation rate, stellar mass, and a number density of galaxy in Mpc scale around that (Chen et al. 2001; Bordoloi et al. 2014; Burchett et al. 2016).
- Our sample is heterogeneous in terms of spectral resolution (i.e., $\lambda/\Delta\lambda \sim 1000 - 27000$) and data quality (i.e., a wide range of S/N ratio). It also should be noted that strong absorption lines ($REW \sim 1 - 2 \text{ \AA}$) in our sample have two possible origins: a “single” dense gas system and a clustering of gas clumps of narrow absorption lines, although we cannot separate them into the two groups with our low-resolution spectra. It is highly required to perform the same analyses based on homogeneous (and higher resolution) spectra taken with same telescope and instrument with a specific observing configuration.

5. SUMMARY

We collected spectra of 13 gravitationally lensed quasars from SDSS Quasar Lens Search catalog as well as from the literature, and investigated the fractional equivalent width difference dEW and ion ratio R_{ion} as a function of the physical separation in the transverse direction D_{tra} . We also constructed simple models with five parameters to reproduce the observed results based on 293 metal absorption lines to investigate the internal structure of the CGM. Our main results are as follows.

- Correlation coefficients between absorption strength (i.e., REW) along sightline pairs are almost same for high-ionized lines (e.g., C IV) and low-ionized lines (e.g., Mg II), although the latter tends to have large scatter at $REW < 1 \text{ \AA}$.
- Typical size of high-ionized absorbers is probably larger than that of low-ionized absorbers because the former has small ion ratio ($R_{\text{ion}} \sim 2\%$) only at larger physical distance between sightlines of lensed images ($D_{\text{tra}} \sim 10 \text{ kpc}$) while the latter has $R_{\text{ion}} \sim 16\%$ at the smaller scale of $D_{\text{tra}} \sim 1 \text{ kpc}$.
- Both high and low-ionized absorbers have almost same values of the fractional equivalent width difference $dEW \sim 0.2$ for a wide range of sightline separations $D_{\text{tra}} \sim 0.1 - 10 \text{ kpc}$, although the latter has a larger scatter of dEW .
- We constructed simple models for the CGM using five parameters; equivalent width distribution as a function of the radius from a spherical cloud center ($EW(r)$), a size (diameter) of each spherical cloud (d), an overall size of the CGM (L), an intensity of equivalent width by diffuse gas (EW_{diff}), and a covering factor (C_f).
- Acceptable ranges of these parameters for high-ions are $d \leq 1 \text{ kpc}$, $L > 100 - 500 \text{ kpc}$ ($L > 500 \text{ kpc}$ is more reasonable), $C_f = 2$, with no diffuse gas or $d \leq 0.5 \text{ kpc}$, $L > 100 - 500 \text{ kpc}$, $C_f = 1$, with a diffuse gas whose equivalent width is about a half the peak value of each spherical cloud. Those for low-ions are $d \leq 1 \text{ kpc}$, $L \geq 500 \text{ kpc}$, $C_f = 1.5$, with no diffuse gas. Both the elliptical and the inverse-proportional functions are acceptable, although the former gives a better result.

Comparing the models and the observations, we placed constraints on the internal structure of the CGM with acceptable ranges for five parameters. Our best model gives a picture of the CGM that is similar to those in the literature: low-ionized absorbers have a complex internal structure consisting of a large number of small-scale clouds, and they are embedded in the diffusely distributed high-ionized regions.

Our results suggest that more detailed analysis using larger samples taken with same telescope/instrument is important to strengthen our conclusion. More lensed quasars will be discovered by deep imaging surveys like the Hyper Suprime-Cam Subaru Strategic Program (HSC-SSP; Aihara et al. (2017)) with follow-up spectroscopic observations. If absorption lines are resolved completely in high-resolution spectra, we can further discuss the internal structure of the CGM based on column density (rather than equivalent width) and velocity structure by applying Voigt profile fitting. We also need to perform deep imaging observations to detect host galaxies of our sample absorption systems to investigate the physical properties of the CGM as a function of the impact parameter from host galaxies of absorbers. By doing so, we will be able to discuss a volume number density of gas clouds as a function of the distance from the host galaxies to improve our current models.

We would like to thank the anonymous referee for valuable comments that helped us to improve the paper. We also would like to thank Christopher Churchill for providing us with the software package, SEARCH. We also would like to Masami Ouchi, Akio Inoue, and Shiro Mukae for their helpful comments and discussions. The research was supported by the Japan Society for the Promotion of Science through Grant-in-Aid for Scientific Research 15K05020 and partially supported by MEXT Grant-in-Aid for Scientific Research on Innovative Areas (No. 15H05894). NK acknowledges supports from the JSPS grant 15H03645. KO acknowledges supports from the JSPS grant 16K05299.

REFERENCES

- Adelberger, K. L., Steidel, C. C., Shapley, A. E., & Pettini, M. 2003, *ApJ*, 584, 45
- Adelberger, K. L., Shapley, A. E., Steidel, C. C., et al. 2005, *ApJ*, 629, 636
- Aihara, H., Armstrong, R., Bickerton, S., et al. 2017, *arXiv:1702.08449*
- Arrigoni Battaia, F., Hennawi, J. F., Cantalupo, S., & Prochaska, J. X. 2016, *ApJ*, 829, 3
- Bergeron, J., & Boissé, P. 1991, *A&A*, 243, 344
- Bordoloi, R., Tumlinson, J., Werk, J. K., et al. 2014, *ApJ*, 796, 136
- Borisova, E., Cantalupo, S., Lilly, S. J., et al. 2016, *ApJ*, 831, 39
- Burchett, J. N., Tripp, T. M., Bordoloi, R., et al. 2016, *ApJ*, 832, 124
- Cantalupo, S., Arrigoni-Battaia, F., Prochaska, J. X., Hennawi, J. F., & Madau, P. 2014, *Nature*, 506, 63
- Chen, H. W., Helsby, J. E., Gauthier, J. R., et al. 2010, *ApJ*, 714, 1521
- Chen, H. W., Wild, V., Tinker, J. L., et al. 2010, *ApJ*, 724, L176
- Chen, H. W., Lanzetta, K. M., & Webb, J. K. 2001, *ApJ*, 556, 158
- Churchill, C. W., Trujillo-Gomez, S., Nielsen, N. M., & Kacprzak, G. G. 2013, *ApJ*, 779, 87
- Churchill, C. W., Vogt, S. S., & Charlton, J. C. 2003, *AJ*, 125, 98
- Churchill, C. W. 1997, Ph.D. Thesis, Univ. California, Santa Cruz
- Ellison, S. L., Ibata, R., Pettini, M., et al. 2004, *A&A*, 414, 79
- Ferland, G. J., Chatzikos, M., Guzmán, F., et al. 2017, *RMxAA*, 53, 385
- Ferland, G. J., Korista, K. T., Verner, D. A., et al. 1998, *PASP*, 110, 761
- Haardt, F., & Madau, P. 2012, *ApJ*, 746, 125
- Hennawi, J. F., Prochaska, J. X., Cantalupo, S., & Arrigoni-Battaia, F. 2015, *Science*, 348, 779
- Hennawi, J. F., Prochaska, J. X., Burles, S., et al. 2006, *ApJ*, 651, 61
- Inada, N., Becker, R. H., Burles, S., et al. 2003, *AJ*, 126, 666
- Inada, N., Burles, S., Gregg, M. D., et al. 2005, *AJ*, 130, 1967

- Inada, N., Oguri, M., Becker, R. H., et al. 2006, *AJ*, 131, 1934
- Inada, N., Oguri, M., Becker, R. H., et al. 2007, *AJ*, 133, 206
- Inada, N., Oguri, M., Shin, Min-Su., et al. 2009, *AJ*, 137, 4118
- Inada, N., Oguri, M., Shin, Min-Su., et al. 2012, *AJ*, 143, 119
- Kacprzak, G. G., Churchill, C. W., & Nielsen, N. M. 2012, *ApJ*, 760, L7
- Kayo, I., Inada, N., Oguri, M., et al. 2010, *AJ*, 139, 1614
- Lanzetta, K. M., & Bowen, D. 1990, *ApJ*, 357, 321
- Lau, M. W., Prochaska, J. X., & Hennawi, J. F. 2016, *ApJS*, 226, 25
- Monier, E. M., Turnshek, D. A., & Lupie, O. L. 1998, *ApJ*, 496, 177
- Nielsen, N. M., Churchill, C. W., & Kacprzak, G. G. 2013, *ApJ*, 776, 115
- Oguri, M., Inada, N., Hennawi, J. F., et al. 2005, *ApJ*, 622, 106
- Oguri, M., Inada, N., Strauss, M. A., et al. 2012, *AJ*, 143, 120
- Prochaska, J. X., Lau, M. W., & Hennawi, J. F. 2014, *ApJ*, 796, 140
- Prochaska, J. X., Hennawi, J. F., Lee, K. G., et al. 2013, *ApJ*, 776, 136
- Prochaska, J. X., Weiner, B., Chen, H. W., Mulchaey, J., & Cooksey, K. 2011, *ApJ*, 740, 91
- Rakic, O., Schaye, J., Steidel, C. C., et al. 2013, *MNRAS*, 433, 3103
- Rakic, O., Schaye, J., Steidel, C. C., & Rudie, G. C. 2012, *ApJ*, 751, 94
- Rubin, K. H. R., Hennawi, J. F., Prochaska, J. X., et al. 2015, *ApJ*, 808, 38
- Rudie, G. C., Steidel, C. C., Trainor, R. F., et al. 2012, *ApJ*, 750, 67
- Smette, A., Robertson, J. G., Shaver, P. A., et al. 1995, *A&AS*, 113, 199
- Steidel, C. C., Erb, D. K., Shapley, A. E., et al. 2010, *ApJ*, 717, 289
- Stern, J., Hennawi, J. F., Prochaska, J. X., & Werk, J. K. 2016, *ApJ*, 830, 87
- Tumlinson, J., Thom, C., Werk, J. K., et al. 2011, *Science*, 334, 948
- Turner, M. L. 2015, Ph.D. Thesis,
- Turner, M. L., Schaye, J., Steidel, C. C., Rudie, G. C., & Strom, A. L. 2015, *MNRAS*, 450, 2067
- Turner, M. L., Schaye, J., Steidel, C. C., Rudie, G. C., & Strom, A. L. 2014, *MNRAS*, 445, 794
- Werk, J. K., Prochaska, J. X., Cantalupo, S., et al. 2016, *ApJ*, 833, 54